Probing Heavy Charged Higgs Boson Using Multivariate Technique at Gamma-Gamma Collider

Ijaz Ahmed[1†] Abdul Quddus[1‡] Jamil Muhammad[2§] Muhammad Shoaib[3¶] Saba Shafaq[4#]

[1]Federal Urdu University of Arts, Science and Technology, Islamabad Pakistan
[2]Sang-Ho College, and Department of Physics, Konkuk University, Seoul 05029, South Korea
[3]Institute of Physics (IoP), The Islamia University of Bahawalpur, Bahawalpur 63100, Pakistan
[4]International Islamic University Islamabad Pakistan

Abstract: The current study explores the production of charged Higgs particles through photon-photon collisions within the context of the Two Higgs Doublet Model, including one-loop-level scattering amplitudes of Electroweak and QED radiation. The cross-section has been scanned for plane (m_{ϕ^0}, $\sqrt{s}$) investigating the process of $\gamma\gamma \to H^+H^-$. Three particular numerical scenarios i.e., low-m_H, non-alignment, and short-cascade are employed. The decay channels for charged Higgs particles are examined using h^0 for low-m_{H^0} and H^0 for non-alignment and short-cascade scenario incorporating the new experimental and theoretical constraints along with the analysis for cross-sections. It reveals that at low energy, it is consistently higher for all scenarios. However, as $\sqrt{s}$ increases, it reaches a peak value at 1 TeV for all benchmark scenarios. The branching ratio of the decay channels indicates that for non-alignment, the mode of decay $W^{\pm}h^0$ takes control, and for short cascade, the prominent decay mode remains $t\bar{b}$, while in the low-m_H the dominant decay channel is of $W^{\pm}h^0$. In our research, we employ contemporary machine-learning methodologies to investigate the production of high-energy Higgs bosons within a 3.0 TeV $\gamma\gamma$ collider. We have used multivariate approaches such as Boosted Decision Trees (BDT), LikelihoodD, and Multilayer Perceptron (MLP) to show the observability of heavy-charged Higgs Bosons versus the most significant Standard Model backgrounds. The purity of the signal efficiency and background rejection are measured for each cut value.

Keywords: LHC, CMS, Charged Higgs, 2HDM, Gamma-Gamma Collider, Multivariate, ILC, CLIC, ANN

DOI: **CSTR:**

I. INTRODUCTION

A neutral Higgs boson was discovered by the ATLAS and CMS collaborations at the Large Hadron Collider (LHC) in 2012 having approximately a mass of 125 GeV, and its properties were consistent with the prediction of Standard Model (SM) Higgs [1−3]. Within the SM framework, gauge bosons acquire their masses due to the Brout–Englert–Higgs mechanism utilizing the concept of electroweak symmetry breaking (EWSB). The SM of particle physics does not provide any indications of charged Higgs bosons. However, theories beyond the SM propose the existence of charged Higgs bosons and are frequently incorporated into theoretical frameworks such as Two-Higgs-Doublet Models (2HDM), supersymmetric models, composite Higgs models, grand unified theories, and axion models. Among all these BSM theories, the two Higgs doublet model is very important due to its structural relevance to many new physics models like MSSM [4, 5], composite Higgs models, and axion models [6, 7]. Depending upon the couplings to the quarks, the types of 2HDMs predict different properties and interactions for charged Higgs bosons. A charged Higgs boson would be a more massive counterpart to the SM $W^{\pm}$ and Z bosons, which are carriers of the weak force. The Higgs sector in 2HDM is extended to incorporate other degrees of freedom that include the prediction of five Higgs candidates of the minimal supersymmetric exten-

Received 9 September 2024; Accepted 18 December 2024

† E-mail: ijaz.ahmed@fuuast.edu.pk
‡ E-mail: abdulqudduskakakhail@gmail.com
§ E-mail: mjamil@konkuk.ac.kr
¶ E-mail: muhammad.shoaib@iub.edu.pk
# E-mail: saba.shafaq@iiu.edu.pk

sion of the SM (MSSM) [8, 9]. From these five Higgs boson candidates, two are CP even neutral states h, H, one is CP odd A state and the remaining two states charge Higgs states $H^{\pm}$. The discovery of any new scalar Higgs boson, either neutral or charged, will be a strong hint towards the physics beyond the SM of particle physics and the immediate sign of an extended Higgs sector.

The photon-photon $(\gamma-\gamma)$ collider which is a proposed experimental facility at the International Linear Collider (ILC). At ILC basically, high-energy electron-positron beams will be collided, which will result in the production of highly energetic photons. The basic idea behind this is that these highly energetic photons will collide with each other and will provide a unique opportunity to study many phenomena such as the production of charged Higgs or other new-physics processes.

So the future e^+e^- and $\gamma\gamma-$ colliders, with high energy and luminosity, offer great potential for discovering charged Higgs bosons. The output rate at a $\gamma\gamma-$ collider could exceed that of e^+e^-- collisions at the tree level. In 2HDM, the $e^+e^- \to H^+H^-$ process has been analyzed at the tree level, while the $\gamma\gamma \to H^+H^-$ process was only studied at the Born level with Yukawa corrections [10, 11]. The primary channels for the pair production of charged Higgs bosons at linear colliders are $e^+e^- \to H^+H^-$ and $\gamma\gamma \to H^+H^-$. Generally, the cross-section for $e^+e^- \to H^+H^-$ is suppressed by s-channel contributions at high energies, which can result in a larger production rate for the $\gamma\gamma \to H^+H^-$ mode compared to the e^+e^- collision mode. However, the s-channel contributions can be enhanced through specific couplings relative to the $\gamma\gamma$ process. The scattering process $e^+e^- \to H^+H^-$ has been extensively studied, incorporating one-loop corrections within the frameworks of both the 2HDM and the Minimal Supersymmetric Standard Model (MSSM). Conversely, the scattering process $\gamma\gamma \to H^+H^-$ has also been analyzed at the one-loop level.

This paper will focus on the multivariate analysis of charged Higgs boson production at the photon-photon collider at the International Linear Collider (ILC). Three benchmark points are selected for numerical examination, each with a $C\!P$-even scalar mass of $125\,GeV$ and couplings consistent with the known Higgs boson. These points are derived from the "non-alignment", "low-m_H", and "short-cascade" scenarios and have been accurately delineated within the constraints of current experimental data and are fully consistent with theoretical constraints [12]. The cross-section is scanned for plane $(\phi^0, \sqrt{s})$, where ϕ^0 is h^0 for low-m_H and H^0 for non-alignment and short-cascade scenarios. Additionally, the polarization effect is also discussed for all scenarios.

II. REVIEW OF TWO HIGGS DOUBLET MODEL

The two scalar doublets are used to acquire masses for gauge bosons and fermions after having their vacuum expectation values (VEVs). The Lagrangian is given by:

$$\mathcal{L}_{2HDM} = \mathcal{L}_{SM} + \mathcal{L}_{Scalar} + \mathcal{L}_{Yukawa} \tag{1}$$

Where $\mathcal{L}_{Scalar}$ is the Lagrangian for two scalar doublets including kinetic blueenergy and scalar potential terms. The Z_2 symmetry is involved to ignore the Flavour Changing Neutral currents (FCNCs), then the transformation for even, $\Phi_1 \to +\Phi_1$, and for odd is $\Phi_2 \to -\Phi_2$. To keep $\mathcal{L}_{Yukawa}$ invariant for fermions under Z_2-symmetry the fermions are coupled with one scalar field:

$$\mathcal{L}_{Yukawa} = -\bar{Q}_L Y_u \tilde{\Phi}_u u_R - \bar{Q}_L Y_d \Phi_d d_R - \bar{L}_L Y_\ell \Phi_\ell \ell_R + h.c \tag{2}$$

In Equation 2 the $\Phi_{u,d,\ell}$ is either Φ_1 or Φ_2, so based on the discrete symmetry of fermions the 2HDM is classified into four types called Type-I, II, III, and IV. The review for this relevant study is discussed here for $C\!P$-conserving 2HDM. If we assume that in the 2HDM the electromagnetic gauge symmetry is present to perform $SU(2)$ rotation on two doublets for alignment of VEVs of two doublets with $SU(2)$ and the $v = 246\,GeV$ will occupy one neutral Higgs doublet [13]. The two complex doublets Φ_1 from SM and Φ_2 from EW symmetry-breaking are used to construct the 2HDM. The scalar potential under the $SU(2)_L \otimes U(1)_Y$ invariant gauge group is defined as

$$\begin{aligned} V_{2HMD} = {} & m_1^2|\Phi_1|^2 + m_2^2|\Phi_2|^2 - \left[m_{12}^2(\Phi_1^\dagger\Phi_2) + h.c\right] \\ & + \frac{\lambda_1}{2}(\Phi_1^\dagger\Phi_2)^2 + \frac{\lambda_2}{2}(\Phi_2^\dagger\Phi_1)^2 \\ & + \lambda_3(\Phi_1^\dagger\Phi_1)(\Phi_2^\dagger\Phi_2) + \lambda_4(\Phi_1^\dagger\Phi_2)(\Phi_2^\dagger\Phi_1) \\ & + \left[\frac{\lambda_5}{2}(\Phi_1^\dagger\Phi_2)^2 + \lambda_6(\Phi_1^\dagger\Phi_1)(\Phi_1^\dagger\Phi_2)\right. \\ & \left. + \lambda_7(\Phi_1^\dagger\Phi_2)(\Phi_2^\dagger\Phi_2) + h.c\right] \end{aligned} \tag{3}$$

In the above Equation 3 the quartic coupling parameters are λ_i $(i = 1,2,3...,7)$ and the complex two doublets are Φ_i $(i = 1,2)$. Hermiticity of the potential forces $\lambda_{1,2,3,4}$ to be real while $\lambda_{5,6,7}$ and m_{12}^2 can be complex. The Paschos-Glashow-Weinberg theorem suggests that a discrete Z_2-symmetry can explain certain low-energy observables [14, 15]. Utilizing this symmetry is crucial to effectively prevent any possibility of FCNCs occurring at the tree level. The Z_2-symmetry requires that $\lambda_6 = \lambda_7 = 0$ and also $m_{12}^2 = 0$. If this is not allowed, i.e., m_{12}^2 is non-zero, then the Z_2-symmetry is softly broken for the translation of $\Phi_1 \to +\Phi_1$ and $\Phi_2 \to -\Phi_2$. The Z_2 assignments produce four 2HDM-types as mentioned earlier [16, 17]. Table 1 demonstrates how fermions bind to each Higgs doublet in

Table 1. In 2HDMs with Z_2-symmetry, Higgs doublets Φ_1,Φ_2 couple to u-type and d-type quarks, as well as charged leptons.

Type	u_i	d_i	ℓ_i
I	Φ_2	Φ_2	Φ_2
II	Φ_2	Φ_1	Φ_1
III	Φ_2	Φ_2	Φ_1
IV	Φ_2	Φ_1	Φ_2

the permitted kinds when flavor conservation is naturally observed.

This work focuses only on Type-I and Type-II 2HDM whereas in Type-I only Φ_2 doublet interacts with both quarks and leptonblues similarly as SM. In Type-II the Φ_1 couples with d-type quarks and leptons while the Φ_2 with only u-type quarks.

After electroweak symmetry breaking of $SU(2)_L \otimes U(1)_Y$, the scalar doublet's neutral components get VEV to be v_j.

$$\Phi_j = \begin{pmatrix} \phi_j^+ \\ \frac{1}{\sqrt{2}}(v_j + \rho_j + i\eta_j) \end{pmatrix}, \qquad (j = 1,2) \tag{4}$$

where ρ_j and η_j are real scalar fields. The quartic coupling parameters $\lambda_1 - \lambda_5$ and mass terms m_1^2, m_2^2 are considered as physical masses of $m_h, m_H, m_A, m_{H^\pm}$ with $\tan\beta = \frac{v_1}{v_2}$ and mixing term $\sin(\beta-\alpha)$. After Z_2-symmetry is broken softly, the parameter m_{12}^2 is given by

$$m_{12}^2 = \frac{1}{2}\lambda_5 v^2 \sin(\beta-\alpha)\cos(\beta-\alpha) = \frac{\lambda_5}{2\sqrt{2}G_F}\left(\frac{\tan\beta}{1+\tan^2\beta}\right) \tag{5}$$

where the last equality is only for the tree level. By considering λ_6 and λ_7 equal to zero concerning Z_2-symmetry, m_{12}^2, $\tan\beta$ and mixing angle α with four Higgs masses, it} is enough to compute a complete model on a physical basis. So, with all this, there are seven independent free parameters to explain the Higgs sector in 2HDM. The terms m_1^2 and m_2^2 are given in the form of other parameters:

$$m_1^2 = m_{12}^2\frac{v_2}{v_1} - \frac{\lambda_1}{2}v_1^2 - \frac{1}{2}(\lambda_3+\lambda_4+\lambda_5)v_2^2 \tag{6}$$

$$m_2^2 = m_{12}^2\frac{v_1}{v_2} - \frac{\lambda_1}{2}v_1^2 - \frac{1}{2}(\lambda_3+\lambda_4+\lambda_5)v_2^2 \tag{7}$$

The phenomenology is dependent upon the mixing angle with angle β. In the limit where $\mathcal{CP}$-even Higgs boson h^0 acts like SM Higgs then it approaches the alignment limit, which is most favored by experimentalists if $\sin(\beta-\alpha)\to 1$ or $\cos(\beta-\alpha)\to 0$. The H^0 acts as gauge-phobic such that its coupling with vector bosons $Z/W^\pm$ is much more suppressed, but when $\cos(\beta-\alpha)\to 1$ the H^0 acts SM-like Higgs boson. For the decoupling limits $\cos(\beta-\alpha)=0$ and $m_{H^0,A^0,H^\pm} >> m_Z$ so at this limit h^0 interacts with SM particles completely appears like the couplings of the SM Higgs boson that contain coupling $3h^0$.

III. CONSTRAINTS FROM THEORY AND EXPERIMENT

The theoretical restrictions of potential unitarity, stability, and perturbativity compress the parameter space of the scalar 2HDM potential. The vacuum stability of the 2HDM limits the V_{2HDM}. Specifically, $V_{2HDM} \geq 0$ needs to be met for all Φ_1 and Φ_2 directions. As a result, the following criteria are applied to the parameters λ_i [18, 19]

$$\lambda_1 > 0 \ , \ \lambda_2 > 0 \ , \ \lambda_3 + \sqrt{\lambda_1\lambda_2} + Min(0, \lambda_4 - |\lambda_5|) > 0 \tag{8}$$

Another set of constraints enforces that the perturbative unitarity needs to be fulfilled for the scattering of longitudinally polarized gauge and Higgs bosons. Besides, the scalar potential needs to be perturbative by demanding that all quartic coefficients satisfy $|\lambda_{1,2,3,4,5}| \leq 8\pi$. The global fit to EW requires $\Delta\rho$ to be $O(10^{-3})$ [20]. This prevents substantial mass splitting between Higgs boson in 2HDM and requires that $m_{H^\pm} \approx m_A, m_H$ or m_h.

Aside from the theoretical restrictions mentioned above, 2HDMs have been studied in previous and continuing experiments, such as direct observations at the LHC or indirect B-physics observables. As a consequence, numerous findings have been amassed since then, and the parameter space of the 2HDM is now constrained by all results obtained. In the Type-I of 2HDM, the following pseudoscalar Higgs mass regions: 310 $\leq m_A \leq$ 410 GeV for m_H = 150 GeV, 335 $\leq m_A \leq$ 400 GeV for m_H = 200 GeV, and 350 $\leq m_A \leq$ 400 GeV for m_H = 250 GeV with $\tan\beta = 10$ have been excluded by the LHC experiment [21]. Furthermore, the $\mathcal{CP}-$odd Higgs mass is bounded as $m_A \geq 350$ GeV for $\tan\beta \leq 5$ [22] and the mass range 170 $\leq m_H \leq$ 360 GeV with $\tan\beta \leq 1.5$ is excluded for the Type-I [23].

The $H^\pm$ mass is constrained by experiments at the LHC and prior colliders, as well as B-physics observables. The BR($b\to s\gamma$) measurement limits the charged Higgs mass in Type-II and IV 2HDM with $m_{H^\pm} \geq 580$ GeV for $\tan\beta \geq 1$ [24, 25]. On the other hand, the bound is significantly lower in Type-I and III of 2HDM [26]. With $\tan\beta \geq 2$, the $H^\pm$ in Type-I and III of 2HDM can be as light as 100 GeV [27, 28] while meeting LEP, LHC, and B-physics constraints [29−33].

IV. COLLIDER SETUP AND BENCHMARK POINTS SCENARIOS

In our study, we concentrate on electron-positron (e^+e^-) collisions, where the center-of-mass energy, represented as √s, is crucial to understanding these interactions. Notably, during these collisions, photons can be emitted due to bremsstrahlung effects and other mechanisms. These emitted photons may subsequently engage in interactions that mimic photon-photon ($\gamma\gamma$) collisions. While such photon interactions can facilitate the production of additional particles, their energy levels are often unpredictable, making them less controllable than the highly precise and defined energy present in e^+e^- collisions. Therefore, our analysis primarily emphasizes the controlled conditions offered by electron-positron collisions, while also acknowledging the potential contributions of radiated photons to particle production.

We have taken three scenarios [12]: non-alignment, short cascade, and low-m_H. All of these are taken for $\mathcal{CP}-$even scalar of mass 125 GeV and couplings are well arranged with observed Higgs boson. The additional Higgs boson searches leave a considerable portion of their parameter space unconstrained, emphasizing the need for further investigation. Validation of potential stability, perturbativity, and unitarity for each BP was performed using `2HDMC 1.8.0` [34].

These benchmark situations, shown in Table 2, are created using a hybrid approach, where the input parameters are specified as $(m_h, m_H, \cos(\beta-\alpha), \tan\beta, Z_4, Z_5, Z_7)$ with softly broken 2HDM of Z_2-symmetry, where the $Z_{4,5,7}$ are quartic couplings in Higgs basis of $O(1)$. The mass of charged Higgs and pseudoscalar Higgs in this basis is obtained as:}

$$Z_i = \frac{1}{4}s_{2\beta}^2[\lambda_1+\lambda_2-2\lambda_3 45]+\lambda_i \tag{9}$$

where i=3,4 or 5

$$Z_6 = -\frac{1}{2}s_{2\beta}[\lambda_1 c_\beta^2-\lambda_2 s_\beta^2-\lambda_{345}c_{2\beta}] \tag{10}$$

$$Z_7 = -\frac{1}{2}s_{2\beta}[\lambda_1 s_\beta^2-\lambda_2 c_\beta^2+\lambda_{345}c_{2\beta}] \tag{11}$$

Table 2. A set of benchmark scenario input parameters that may be utilized to actualize the 2HDM in Hybrid Basis.

Scenario	$\mathbf{m_{h^0}}$ [GeV]	$\mathbf{m_{H^0}}$ [GeV]	$\mathbf{c_{\beta-\alpha}}$	$\mathbf{Z_4}$	$\mathbf{Z_5}$	$\mathbf{Z_7}$	$\mathbf{t_\beta}$
BP-1	125	150...600	0.1	−2	−2	0	1...20
BP-2	125	250...500	0	−1	1	−1	2
BP-3	125	250...500	0	2	0	−1	2
BP-4	65...120	125	1.0	−5	−5	0	1.5

where $\lambda_{345} = \lambda_3+\lambda_4+\lambda_5$. Since there are five nonzero λ_i and seven nonzero Z_i, there must be two relations

$$m_{A^0}^2 = m_{H^0}^2 s_{\beta-\alpha}^2 + m_{h^0}^2 c_{\beta-\alpha}^2 - Z_5 v^2 \tag{12}$$

$$m_{H^\pm}^2 = m_{A^0}^2 - \frac{1}{2}(Z_4-Z_5)v^2 \tag{13}$$

A. Non-alignment

We consider a scenario characterized by non-alignment (specifically $(c_{\beta-\alpha}\neq 0)$. This scenario emphasizes the search for the heavier CP-even Higgs state, (H), in Standard Model final states, including the decay $(H\to hh)$. The other two Higgs bosons, (A) and $(H^\pm)$ (which are assumed to be mass-degenerate), are sufficiently decoupled to establish a small hierarchy: $(m_h = 125\,GeV \le m_H \le m_A = m_{H^\pm})$. For $(m_H > 150\,GeV)$, this setup can be realized by choosing $(Z_4 = Z_5 = -2)$, resulting in $(m_{H^\pm})$ values that comply with the $(b\to s\gamma)$ constraint in Type-II models. The value of $(c_{\beta-\alpha})$ is fixed close to the maximum allowed by LHC Higgs constraints: $(c_{\beta-\alpha}=0.1)$ for Type-I couplings and $(c_{\beta-\alpha}=0.01)$ for Type-II couplings. As a result, we treat (m_H) and $(\tan\beta)$ as free parameters. These choices lead to an excellent fit for light Higgs signal rates over a substantial region of the $((m_H, \tan\beta)$ parameter space.

B. Low-m_H

Both h and heavy Higgs H are light in the low-m_H, but $m_H = 125$ GeV behaves like SM. For $s_{\beta-\alpha}\to 0$ limit compatibility, the lighter CP-even higgs boson must have a highly suppressed coupling to the vector bosons, as $m_h < m_H$. Since the hybrid quartic basis $Z_4 = Z_5 = -5$ is consistent with the restrictions from (flavor physics) light-charged Higgs boson of the order of m_H, especially in Type-II couplings, it is used to decouple the other two Higgs states, A and $H^\pm$. Searches $h\to bb, \tau^+\tau^-$ at the LHC confine the parameter space for $90 < m_h < 120$ GeV, resulting in an upper bound on $tan\beta$ that depends weakly on limit $c_{\beta-\alpha} << 1$. In this study, we are concerned with $\tan\beta = 1.5$ as a function of m_h, and we fix it with $c_{\beta-\alpha}=1$.

C. Short Cascade

By setting $c_{\beta-\alpha}$ to zero for the precise alignment, we take into account a brief cascade scenario. The $H\to ZA$ or $H\to W^\pm H^\mp$ decay mode can be obtained by altering the mass hierarchy, which can be dominant in the mass window of 250 GeV$< m_H <$ 350 GeV and causes a "small cascade" of Higgs-to-Higgs decay. Degeneracies for hybrid basis Z_4, Z_5 are chosen properly, and two of the three non-SM-like Higgs masses are chosen to be identical by fixing $\tan\beta = 2$ for a single free parameter space. The hybrid basis choice of $Z_4 = -1$ and $Z_5 = 1$ may be used to

achieve the low$-m_A$ case. For m_h near 250 GeV, the decay $H \to AA$ can be open with a rate that can be varied by adjusting Z_7, which in this instance is $Z_7 = -1$ that satisfies stability criteria. With all other parameters held constant, $Z_4 = 2$ and $Z_5 = 0$ can be chosen to create a mass hierarchy $m_{H^\pm} < m_A = m_H$. For very low $m_{H^\pm}$, this condition results in novel decay modes $H \to W^\pm H^\mp$, where $H \to H^+H^-$.

The mass hierarchy is considered for these benchmark points along with the type of the 2HDMs, shown in Table 3. In Table 2, $t_\beta = \tan\beta$ and $c_{\beta-\alpha} = \cos(\beta-\alpha)$.

V. THE LEADING ORDER CROSS-SECTION OF CHARGED HIGGS PRODUCTION

Analytical formulations of the cross-section of the e^+e^- collider for charged Higgs pair generation are presented in this section. The process used in this paper is given as:

$$\gamma(k_1,\mu)\ \ \gamma(k_2,\nu) \longrightarrow H^+(k_3)\ \ H^-(k_4) \tag{14}$$

where $k_a (a = 1,....,4)$ represents the four momenta. Three different diagrams at the tree level are topologically distinct because of photon couplings as shown in Figure 1. The total Feynman amplitude is given by:

$$\mathcal{M} = \mathcal{M}_{\hat{q}} + \mathcal{M}_{\hat{t}} + \mathcal{M}_{\hat{u}} \tag{15}$$

where $\mathcal{M}_{\hat{q}}, \mathcal{M}_{\hat{t}}$ and $\mathcal{M}_{\hat{u}}$ are amplitudes of quartic couplings, t-channel, and u-channel Feynman diagrams respectively. The relations for these channels are given as follows:

$$\mathcal{M}_{\hat{q}} = 2ie^2 g^{\mu\nu}\epsilon_\mu(k_1)\epsilon_\nu(k_2) \tag{16}$$

$$\mathcal{M}_{\hat{t}} = \frac{ie^2}{\hat{t}-m_{H^+}^2}(k_1-2k_4)^\nu\epsilon_\nu(k_2)(k_2+k_3-k_4)^\mu\epsilon_\mu(k_1) \tag{17}$$

$$\mathcal{M}_{\hat{u}} = \frac{-ie^2}{\hat{u}-m_{H^+}^2}(k_1-2k_4)^\mu\epsilon_\mu(k_1)(k_1+k_3-k_4)^\nu\epsilon_\nu(k_2) \tag{18}$$

where the Mandelstam variables are represented by $\hat{t} = (k_1-k_3)^2$ and $\hat{u} = (k_2-k_4)^2$. After calculating the square of the total amplitude and summing all the foregoing matrices yields the lowest order amplitude.

$$M = \sum_{i=1}^{3} M_i \tag{19}$$

The scattering amplitude is calculated numerically in the center of the mass frame, where the four-momentum and scattering angle are indicated by (k,θ). In the center of mass energy, the energy (k_i^0) and momentum $(\vec{k}_i)$ of incoming and outgoing particles are:

$$k_1 = \frac{\sqrt{s}}{2}(1,0,0,1) \quad , \quad k_2 = \frac{\sqrt{s}}{2}(1,0,0,-1) \tag{20}$$

$$k_3 = (k_3^0, |\vec{k}|\sin\theta, 0, |\vec{k}|\cos\theta) \tag{21}$$

$$k_4 = (k_4^0, -|\vec{k}|\sin\theta, 0, -|\vec{k}|\cos\theta) \tag{22}$$

$$k_3^0 = \frac{s+m_i^2-m_j^2}{2\sqrt{s}} \quad , \quad k_4^0 = \frac{s+m_j^2-m_i^2}{2\sqrt{s}} \tag{23}$$

$$|\vec{k}| = \frac{\lambda(s,m_{H^+}^2,m_{H^-}^2)}{\sqrt{s}} \tag{24}$$

Table 3. Mass hierarchy for BP's with 2HDM types used in calculations of cross-section and decay width of charged Higgs.

Scenarios	BP's	2HDM-Type	Mass Hierarchy
Non-alignment	BP-1	I	$m_{H^0} < m_{H^\pm} = m_{A^0}$
Short Cascade	BP-2	I	$m_{A^0} < m_{H^\pm} = m_{H^0}$
Short Cascade	BP-3	I	$m_{H^\pm} < m_{A^0} = m_{H^0}$
Low-$\mathbf{m_H}$	BP-4	II	$m_{h^0} < m_{H^\pm} = m_{A^0}$

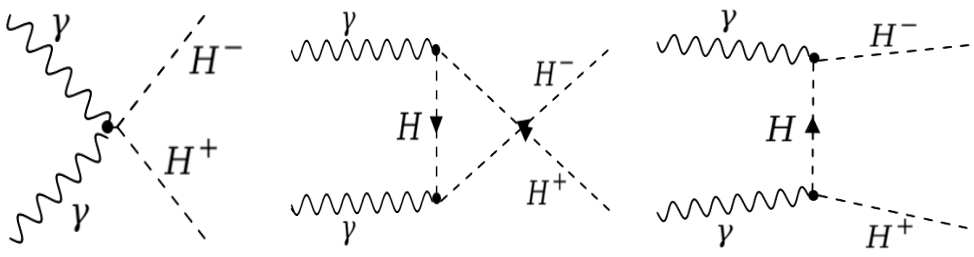

Fig. 1. The tree-level Feynman diagrams for the process $\gamma\gamma \to H^+H^-$.

where m_i^2 is the mass of relevant particles. The cross-section is calculated by taking the flux of incoming particles and the integral over the phase space of outgoing particles is given by:

$$\hat{\sigma}_{\gamma\gamma\to H^+H^-}(s) = \frac{\lambda(s, m_{H^+}^2, m_{H^-}^2)}{16\pi s^2} \sum_{pol} |M|^2 \tag{25}$$

In above expression, the $\lambda(s, m_{H^+}^2, m_{H^-}^2)$ is the Källen function relevant to phase space of outgoing $H^{\pm}$. The total integrated cross section for the e^+e^--collider could be calculated by:

$$\sigma(s) = \int_{x_{min}}^{x_{max}} \hat{\sigma}_{\gamma\gamma\to H^+H^-}(\hat{s}; \hat{s} = z^2 s) \frac{dL_{\gamma\gamma}}{dz} dz \tag{26}$$

where s and $\hat{s}$ are the C.M. energy in e^+e^--collider and subprocess of $\gamma\gamma$, respectively. The value of x_{min} represents the minimum amount of energy needed to generate a pair of charged Higgs particles and is given by $x_{min} = (m_{H^+} + m_{H^-})/\sqrt{s}$, where the x_{max} is 0.83 [35]. The distribution function of the photon luminosity is:

$$\frac{dL_{\gamma\gamma}}{dz} = 2z \int_{x_{min}}^{x_{max}} \frac{dx}{x} F_{\gamma/e}(x) F_{\gamma/e}\left(\frac{z^2}{x}\right) \tag{27}$$

The energy spectrum of Compton back-scattered photons, $F_{\gamma/e}(x)$ is characterized by the electron beam's longitudinal momentum [35].

VI. NUMERICAL RESULTS AND DISCUSSIONS

The numerical results of generating charged Higgs boson via photon-photon collisions are thoroughly examined in the context of 2HDM including QED radiations. Cross sections at the tree level are calculated numerically for each benchmark scenario as a function of the C.M. energy and the Higgs boson mass. Polarization distributions are presented to improve the production rate by considering longitudinal polarizations of initial beams. Decay pathways of the charged Higgs boson are under study for relevant scenarios.

In our work, for analytical and numerical evaluation, we have used `MadGraph5 v3.4.2` [36] for the calculations of the cross-sections, and `2HDMC 1.8.0` [37] for the branching ratio and total decay width. The `GnuPlot` [38] is used for the graphical plotting.

In an electron-positron e-e+ collider, the longitudinally polarized beam cross-section can be expressed as

$$\begin{aligned}\sigma_{P_{e^+},P_{e^-}} = \frac{1}{4}\{&(1+P_{e^+})(1+P_{e^-})\sigma_{RR} + (1-P_{e^+})(1-P_{e^-})\sigma_{LL} \\ &+ (1+P_{e^+})(1-P_{e^-})\sigma_{RL} + (1-P_{e^+})(1+P_{e^-})\sigma_{LR}\}\end{aligned} \tag{28}$$

In electron-positron e-e+ colliders, beam polarization configurations are crucial for optimizing the experimental conditions and enhancing the detection of specific processes, referring to the orientation of the spins of the colliding particles, which can be manipulated to improve the signal-to-background ratio in particle interactions. There are primarily two types of polarization configurations used in e-e+ colliders: Longitudinal Polarization, where both the electron and positron beams are polarized along the direction of the beam (longitudinally), either parallel or antiparallel, leading to typical configurations such as Right-Right (RR) where both beams are right-polarized, Left-Left (LL) where both beams are left-polarized, Right-Left (RL) where the electron beam is right-polarized and the positron beam is left-polarized, and Left-Right (LR) where the electron beam is left-polarized and the positron beam is right-polarized; notably, the RL and LR configurations are particularly advantageous in the context of the Standard Model, as they help enhance the production rate of certain particles, such as the Higgs boson and Z boson while minimizing unwanted background processes. The second configuration, Transverse Polarization, involves polarizing the beams perpendicular to the beam direction (not the case here), which, although less commonly used than longitudinal polarization, can provide benefits in specific scattering processes or studies of the spin structure of particles. As in Figure 2 the cross-section for the process $\gamma\gamma \to H^+H^-$ is shown for the C.M energy of 3 TeV for three types of polarization; right handed RR $(++)$, oppositely-polarized RL $(+-)$ and unpolarized beam UU. The cross-section is the same for the polarization modes of $\sigma^{+-} = \sigma^{-+}$. In Figure 2 it can be seen that the cross-section is higher for UU and RR for low $\sqrt{s}$ and gradually decreases. But for the RL mode of polarization, the cross-section reaches a peak value and then gradually decreases. As we can see the cross-section is not enhanced for RR and UU at higher energies but it does only for RL.

In Figure 3 for both BPs, the cross-section changes slowly with the mass of h^0 and H^0 because of the small range of charged Higgs mass. For both UU and RR modes of polarization the cross-section decreases with C.M energy and for RL mode it reaches a peak value and then decreases. The cross-section σ decreases for $\sqrt{s}$ when $m_{H^{\pm}} << \sqrt{s}/2$.

VII. DECAYS OF CHARGED HIGGS BOSON

To investigate the process in a collider, we must first identify all potentially charged Higgs products. The total decay widths of the charged Higgs boson versus the mass of Higgs h^0 or H^0 are plotted for all BPs. As expected, the mass of the charged Higgs boson increases with increasing neutral Higgs mass m_{ϕ^0} under all circumstances. The decay widths are highly sensitive to the mass hier-

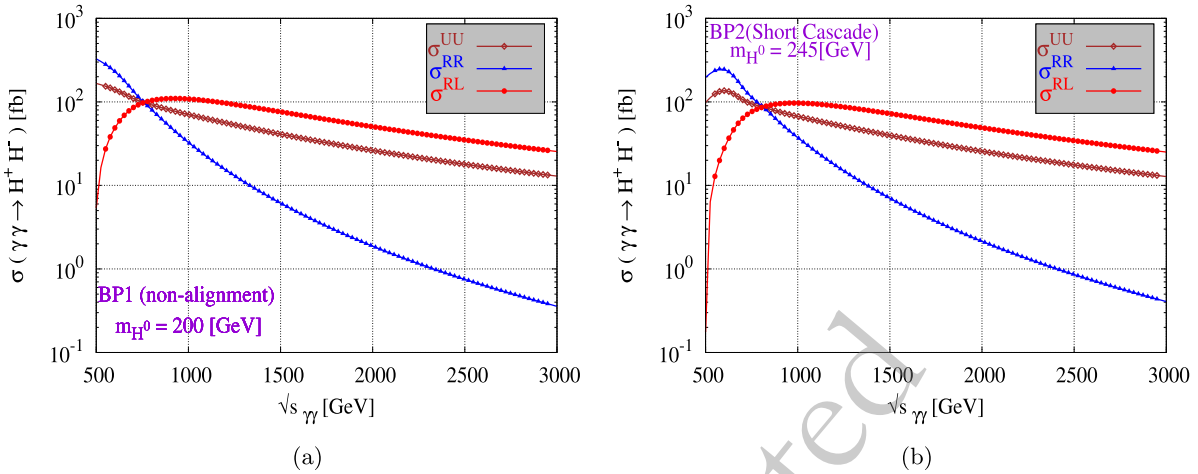

Fig. 2. (color online) Integrated cross-section for $\gamma\gamma \to H^+H^-$ as a function of $\sqrt{s}$ for BP-1 in (a) and BP-2 in (b), respectively

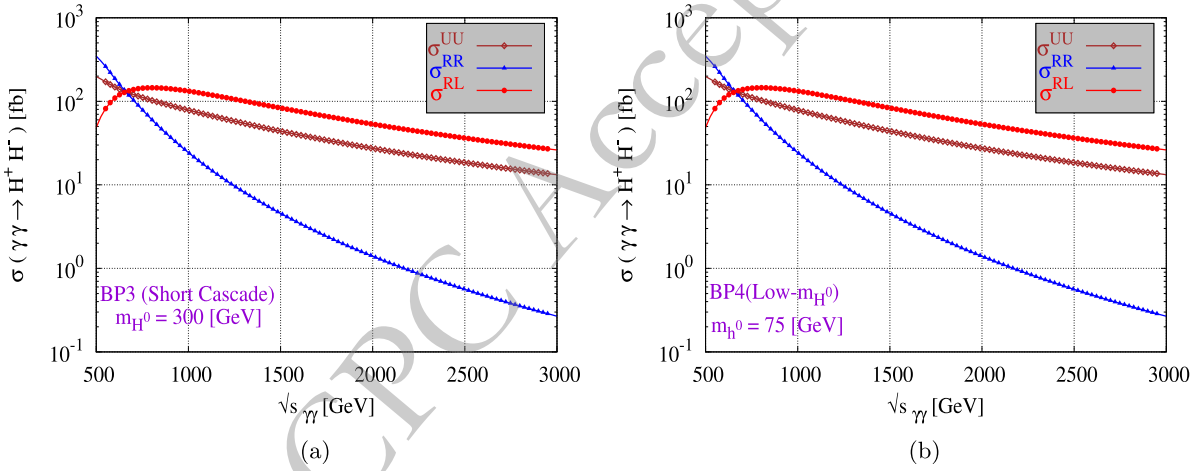

Fig. 3. (color online) Integrated cross-section for process $\gamma\gamma \to H^+H^-$ as a function of $\sqrt{s}$ for BP-3 in (a) and BP-4 in (b), respectively.

archy and mass splitting. Shrinking of the decay width is observed when $m_{H^0} - m_{H^\pm}$, the mass splitting is minimal, as shown in Figure 4. The decay width for BP-1 decreases from 8.66 to 1.42 when the $m_{H^\pm}$ goes from 379 to 691 GeV. For BP-2, the decay width increases from 4.38 to 5.22 for $m_{H^\pm}$ in the range of $250 < m_{H^\pm} < 550$ GeV. The $\Gamma_{H^\pm}$ for BP-3 increases from 3.5×10^{-5} to 4.28 when $m_{H^\pm}$ runs from 48.75 to 436 GeV. For the last BP-4, the decay width decreases from 60 to 58 for change of $m_{H^\pm}$ from 558 to 564 GeV.

We showed the dominant modes of BR for $H^\pm$ as a function of h^0 and H^0 for all scenarios. The $W^\pm H^0$ channel is the primary decay mode for $H^\pm$ in BP-1, as shown in Figure 5. The sub-dominant channels are as follows: $t\bar{b}$ and $W^\pm h^0$ for charged Higgs for BP-1, other suppressed channels are $c\bar{s}$ and $t\bar{s}$ for range $m_{H^0} < 500$ GeV. The mode of decay $W^\pm h^0$ takes control when $BR(H^\pm \to W^\pm H^0)$ decreases at larger values of m_{H^0}. So for $BR(H^\pm \to W^\pm h^0)$ range rises from 1.2 to 66.3% of $150 < m_{H^0} < 600$ GeV. The process H^0 to W^+W^- is also

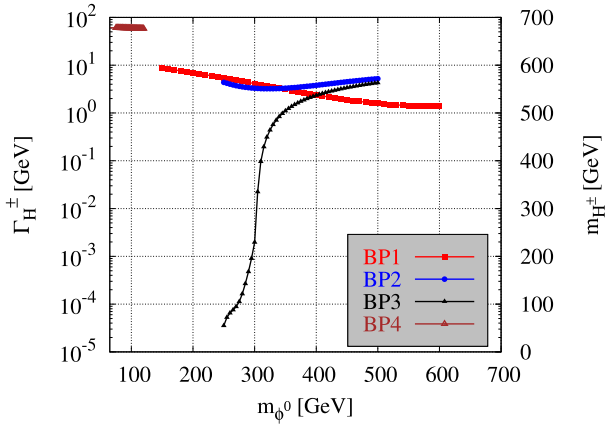

Fig. 4. (color online) Total decay widths for charged Higgs boson $H^\pm$ for all benchmark points.

another dominant decay mode with BR of 88.7 to 50.2%, and with hadronic decay of $W^\pm$ has 12-jets in the final state.

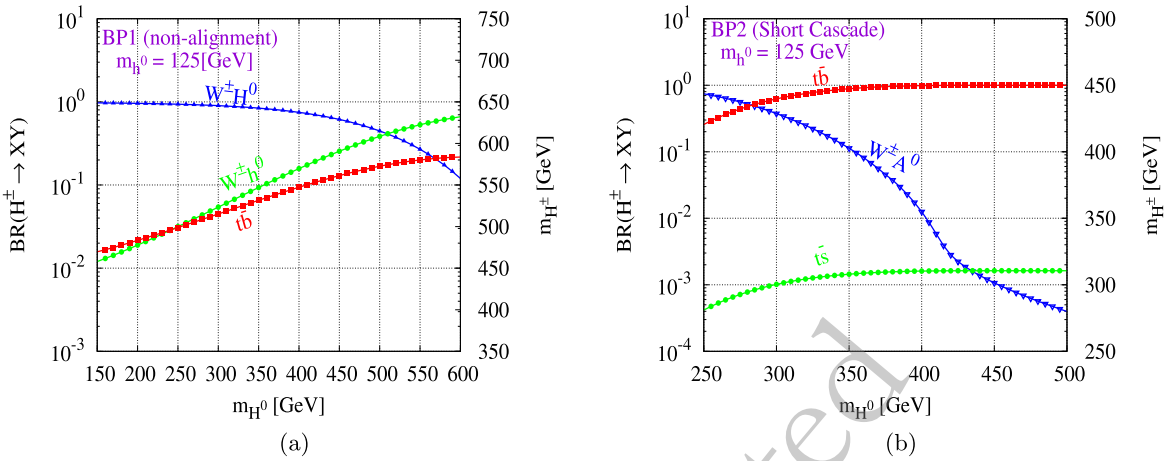

Fig. 5. (color online) The BR of $H^{\pm}$ predicted in BP-1 from (a) and BP-2 in (b), respectively. For modes, BR is less than 10^{-4} are omitted for clarity.

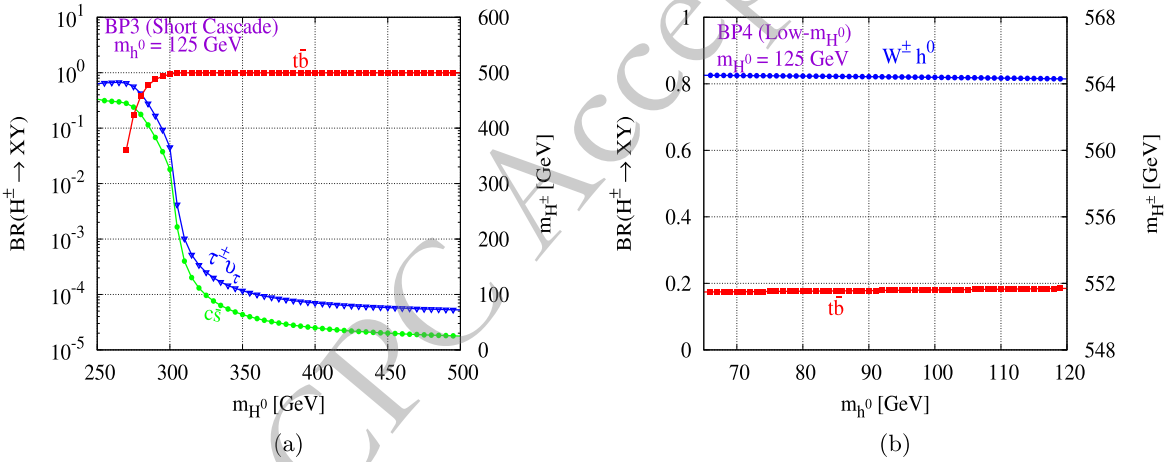

Fig. 6. The BR of $H^{\pm}$ predicted in BP-3 from (a) and BP-4 in (b), respectively. For modes, BR is less than 10^{-4} are omitted for clarity.

In the BP-2 and BP-3, as shown in Figure 5 and Figure 6 respectively, as $m_{H^{\pm}} > m_t + m_b$ the BR of 100% prominent decay mode is $H^{\pm} \to t\bar{b}$. The suppressed decay modes of $m_{H^0} < 300$ GeV are for $W^{\pm}A^0$ and $t\bar{s}$ in both BP-2 and BP-3; the $t-$quark decay is ideal for the reconstruction of the process at $m_{H^0} > 300$ GeV. So for process $t \to Wb, W \to q\bar{q}(l\nu_l)$ gives $H^{\pm}$ trace at the detector which can be tagged with 8-jets and 2-b-tagged jets. For BP-4, shown in Figure 6, for a range of $65 < m_{h^0} < 120$ GeV the dominant channel is $W^{\pm}h^0$ because for $\sin(\beta-\alpha)=0$ it leads to 100%. 4-jets and 4-b-tagged jets can be used to tag the process.

VIII. MULTIVARIATE ANALYSIS FOR CHARGED HIGGS PRODUCTION

An integrated ROOT framework for parallel running and computation of several multivariate categorization algorithms is called the "Toolkit for Multivariate Analysis" [39], which categorizes using two sorts of events: signal and background. TMVA especially has many applications in high energy physics for the complex multi-particle final state. To train the classifiers, a set of events with well-defined event types is inserted into the Factory. The event samples for signal and background can either be read using a tree-like structure or a plain text file using a defined structure. All variables that are supposed to separate signal and background events must be known by the Factory. Cuts are applied on signal and background trees separately.

We represent three classifiers in our work; Boosted Decision Tree (BDT), LikelihoodD (Decorrelation), and MLP. In BDT a selection Tree is a tree-like structure that illustrates the different outcomes of a choice using a branching mechanism. An event is categorized as either a signal or a background event by passing or failing to pass a condition (cut) on a certain node until a choice is reached. The "root node" of the decision tree is used to find these cuts. The node-splitting process concludes when the BDT algorithm specifies minimal events

(`NEventsMin`). The final nodes (leaves) are classified according to their "purity" (p). The value for signal or background (usually +1 for signal and 0 or −1 for background) depends on whether p is greater than or less than the stated number, e.g., +1 if $p > 0.5$ and −1 if $p < 0.5$ [40]. To differentiate between the background class and signal, a labeling process is carried out. All occurrences with a classifier output $y > y_{cut}$ are labeled as a signal, while the rest are classified as background. The purity of the signal efficiency $\epsilon_{sig,eff}$ and background rejection $(1-\epsilon_{bkg,eff})$ are evaluated for each cut value of y_{cut} [41]. The ADA-Boost algorithm re-weights every misclassified event candidate. The new candidate weight consists of the one used in the former tree multiplied by $\alpha = 1-\Delta_m/\Delta_m$, where Δ_m is the misclassification error. This leads to an increase in the weight and therefore an increase in the candidate's importance when searching for the best separation values. The weights of each new tree are based on the ones of its predecessor [42]. An Artificial Neural Network (ANN) comprises linked neurons, each with its weight. To speed up the processing, a reduced layout can be used as well, the so-called multilayer perception (MLP). The network consists of three kinds of layers. The input layer, consisting of n_{var} neurons and a bias neuron, many deep layers containing a user-specified number of neurons (set in the option `HiddenLayers`) plus a bias node, and an output layer and each of the connections between two neurons carries a weight.

For event j, the likelihood ratio $y_L(j)$ is defined by

$$y_L(j) = \frac{L_S(j)}{L_S(j)+L_B(j)} \tag{29}$$

where the likelihood of a candidate to be signal/background may be determined using the following formula

$$L_{S/B}(j) = \prod_{i=1}^{n_{var}} P_{S/B,i}(x_i(j)) \tag{30}$$

where $P_{S/B,i}$ is the PDF for the ith input variable x_i. The PDFs are normalized to one for all i:

$$\int_{\infty}^{-\infty} P_{S/B,i}(x_i)dx_i = 1 \tag{31}$$

The projective likelihood classifier has a major drawback in that it does not use correlation among the discriminating input variables. In the realistic approach, it does not provide an accurate analysis and leads to performance loss. Even other classifiers underperform in the presence of variable correlation. Linear Correlation was used to quantify the training sample by obtaining the square root of the covariant matrix. The square root of the matrix C is C', which when multiplied by itself yields $C : C = (C')^2$. As a result, TMVA employs diagonalization of the (symmetric) covariance matrix provided by:

$$D = S^T C S \implies C' = S\sqrt{D}S^T \tag{32}$$

D is the diagonal matrix, while S denotes the symmetric matrix. The linear decorrelation is calculated by multiplying the starting variable $\mathbf{x}$ by the inverse of C'.

$$\mathbf{x} \mapsto (C')^{-1}\mathbf{x} \tag{33}$$

Only linearly coupled and Gaussian distributed variables have full decorrelation. In this work, the signal and background events are taken to be 50000 with applied cuts:

$$P_T^{Jet} > 30\,GeV \ , \ \eta_{Jet} < 2 \ , \ N_{Jet} \le 6 \ ,$$
$$\Delta R < 0.4 \ , \ E_T^{Missing} < 120\,GeV$$

The curve of background rejection against signal efficiency provides a reasonable estimate of a classifier's performance. A classifier's performance is measured by the area under the signal efficiency versus the background rejection curve, so the bigger the area, the better a classifier's predicted separation power, as shown in Figure 7. The values of area under the curve (AUC) for Figure 7. Table 4 shows that the best classifier among all is the MLP and BDT, improved after applying cuts and gave the largest area under the curve. We used 800 trees to improve the BDT's performance, with node splitting at the 2.5% event threshold. Max tree depth set at 3. Trained using Adaptive Boost with a learning rate of $\beta = 0.5$ parent node and the sum of the indices of the two daughter nodes are compared to optimize the cut value on the variable in a node. For the separation index, we use the *Gini Index*. Finally, the variable's range is evenly graded into 20 cells. The signal values are taken to be 1 and background values approach 0.

The Figures 8, 9 and 8 have been specifically generated for Benchmark Point 1 (BP1) at center-of-mass energy $\sqrt{s}$ = 3 TeV, while at 3000 $fb^{-}1$ ensuring that the results accurately reflect the expected physical behaviors

Table 4. MVA Classifier Area Under (AUC) the Curve with cuts and without cuts values

MVA Classifier	AUC (with cut)	AUC (without cut)
MLP	0.958	0.922
BDT	0.957	0.925
LikelihoodD	0.941	0.896

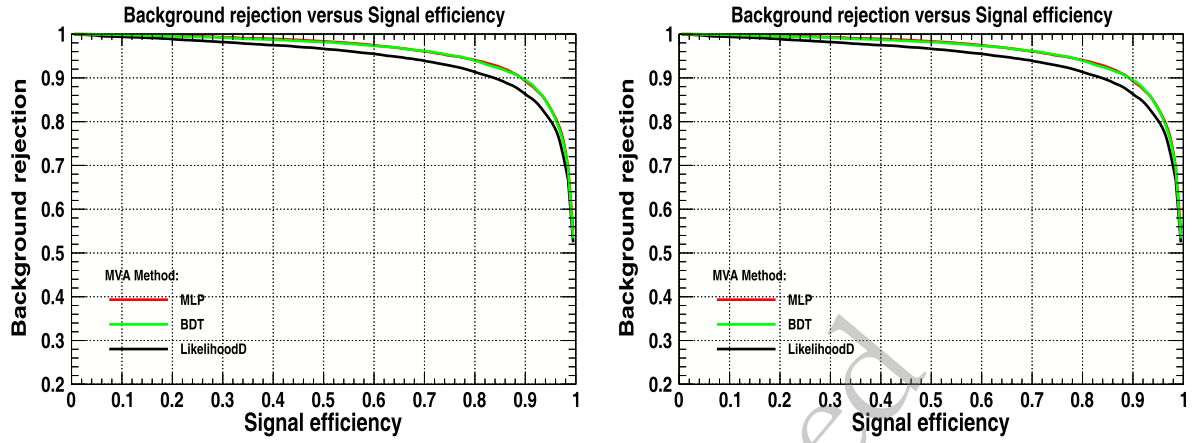

(a) (b)

Fig. 7. (color online) Background Rejection vs Signal Efficiency with applying cuts (a) and without applying cuts (b), respectively.

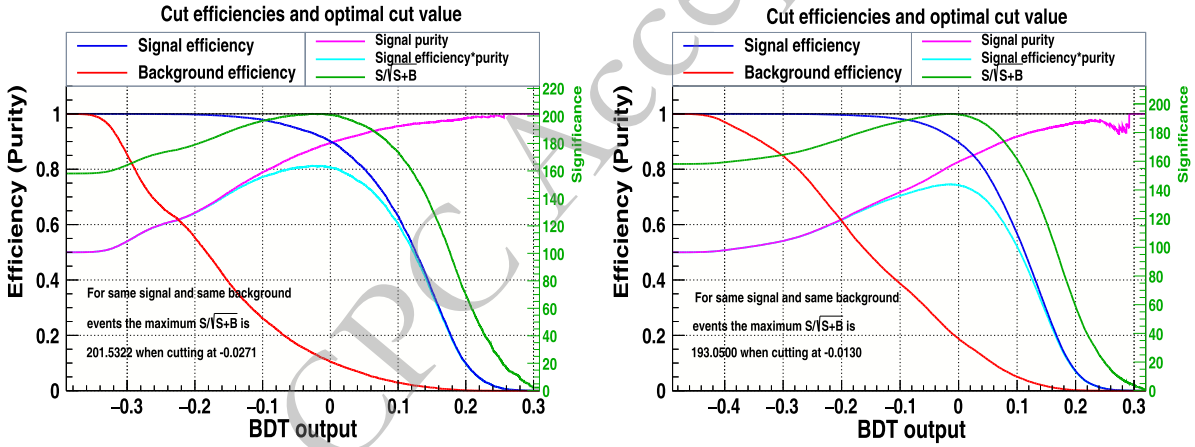

(a) (b)

Fig. 8. (color online) BDT signal significance with applying cuts (a) and without applying cuts (b) respectively.

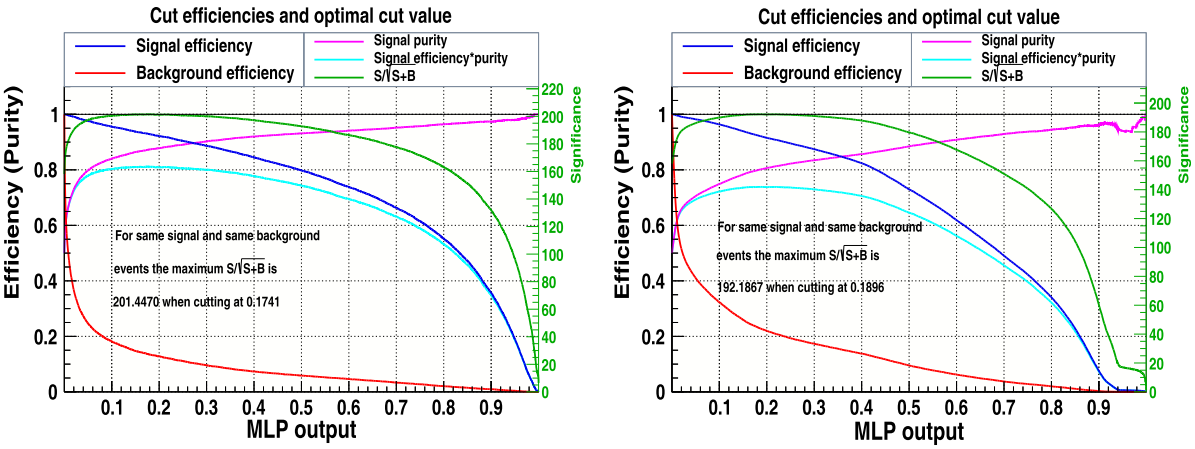

(a) (b)

Fig. 9. (color online) MLP Signal Significance with applying cuts (a) and without applying cuts (b) respectively.

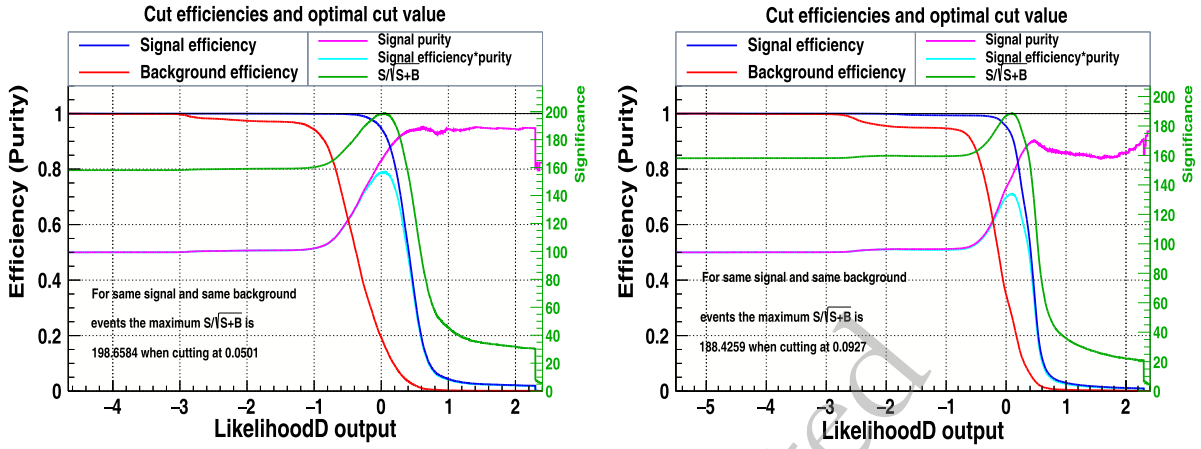

(a) (b)

Fig. 10. (color online) LikelihoodD Signal Significance with applying cuts (a) and without applied cuts (b) respectively.

and interactions at this energy scale under the defined experimental conditions. Figure 8 depicts that the signal significance, $S/\sqrt{S+B}$, of the classifier is improved by applying cuts with an optimal cut of -0.0271. Similarly, Figure 9 shows the best classifier that is improved by applying cuts with an optimal cut value of 0.1741, and the signal efficiency is also higher than without applied cuts. The LikelihoodD signal significance is shown in Figure 10, has been improved by applied cuts with the optimal cut of 0.0501.

IX. CONCLUSION

The simplest extension of SM is 2HDM containing charged Higgs Boson and the exact measurement of its nature and corresponding model parameters are crucial for the discovery. The pair production is one of the best channels that provided the observable signal in the vast range of parameters in 2HDM.

The generation rates of incoming beams are investigated in various polarization collision patterns. The cross-section can be increased twice by oppositely polarized beams of photons at high energies and right-handed polarized beams of photons at low energies as shown in the figures of the cross-section. For BP-1 at the $\sqrt{s} = 3\,TeV$ the $\sigma^{UU} = 12.92 \pm 8.1 \times 10^{-06}$ fb, for $\sigma^{RR} = 0.3568 \pm 4.6 \times 10^{-07}$ fb and for $\sigma^{RL} = 25.48 \pm 1.6 \times 10^{-05}$ fb. For BP-2 the cross section for $\sigma^{UU} = 12.76 \pm 8.03 \times 10^{-06}$ fb, $\sigma^{RR} = 0.4067 \pm 5.3 \times 10^{-07}$ fb and for $\sigma^{RL} = 25.11 \pm 1.8 \times 10^{-05}$ fb at the center of mass energy $3\,TeV$. The cross section at $3\,TeV$ for BP-3 for different polarizations is $\sigma^{UU} = 13.22 \pm 9.1 \times 10^{-06}$ fb, $\sigma^{RR} = 0.2674 \pm 3.2 \times 10^{-07}$ fb and $\sigma^{RL} = 26.17 \pm 1.7 \times 10^{-05}$ fb respectively. In the Low-m_H scenario for BP-4 the cross section for polarized beams is $\sigma^{UU} = 13.23 \pm 9.1 \times 10^{-06}$ fb, $\sigma^{RR} = 0.2673 \pm 3.2 \times 10^{-07}$ fb and for $\sigma^{RL} = 26.19 \pm 1.7 \times 10^{-05}$ fb at $\sqrt{s} = 3\,TeV$ respectively. So we concluded that for all BP's, the cross-section is low at high energy for UU and RR polarized beams of photons, while high for RL at high energy.

For each scenario, the charged Higgs Boson reconstruction has been provided, and its prominent decay modes have been examined. The branching ratio of the decay channel for non-alignment, the bosonic decay channel $H^{\pm} \to W^{\pm}H^0$ is the dominant while in the low$-m_H$ scenarios the bosonic decay of $W^{\pm}h^0$ is dominant rising to 66.3%. The 100% dominant decay channel in a short-cascade scenario is $H^{\pm} \to t\bar{b}$ that concludes the t decay is the ideal candidate for the reconstruction of the process. Limited phase space and alignment constraints restrict bosonic decay channels.

Our Machine Learning models for Multivariate Analysis results are improved by applying cuts. The signal efficiency ($\epsilon_{Sig,eff}$) and background rejection ($1-\epsilon_{Bkg,eff}$) are increased when cuts are applied to the MLP, BDT, and LikelihoodD classifiers. The area under the curve (AUC) is increased for MLP to 3.9%, for BDT it increased to 3.46%, and the LikelihoodD increased up to 5.02% which shows that the LikelihoodD is the more efficient classifier for signal efficiency and background rejection. The signal significance is increased for MLP to 4.81%, for the BDT to 4.39%, and for LikelihooD, it is increased to 5.43% by applying cuts. The significance values obtained with cuts demonstrate how well these models can separate charged Higgs production-related background events from signal occurrences. These cuts most likely aid in lowering background noise, enhancing overall performance, and separating signal events associated with charged Higgs generation. This consistency upholds the validity of the selected machine-learning approaches and increases trust in the outcomes.

ACKNOWLEDGEMENTS

We gratefully acknowledge support from the Simons Foundation and member institutions. The current submitted version of the manuscript is available on the arXiv pre-prints home page

STATEMENTS AND DECLARATIONS

Competing Interests The authors have no relevant financial or non-financial interests to disclose.

Availability of data and materials Data sharing does not apply to this article as no datasets were generated or analyzed during the current study.

References

[1] Observation of a new particle in the search for the Standard Model Higgs boson with the ATLAS detector at the LHC, ATLAS, Collaboration, arXiv preprint arXiv: 1207.7214, (2012)

[2] Observation of a new boson at a mass of 125 GeV with the CMS experiment at the LHC, CMS Collaboration, arXiv preprint arXiv: 1207.7235, (2012)

[3] Precise determination of the mass of the Higgs boson and tests of compatibility of its couplings with the standard model predictions using proton collisions at 7 and 8 TeV, Collaboration, CMS, Eur. Phys. J. C, (2015)

[4] Prospects for charged Higgs searches at the LHC., Arhrib, A and Hernandez-Sanchez, J and Mahmoudi, F and Santos, R and Akeroyd, A and Moretti, S and Yagyu, K and Yildirim, E and Khater, W and Krawczyk, M and others, European Physical Journal C–Particles & Fields, (2017)

[5] Neutral currents and the Higgs mechanism, Ross, DA and Veltman, M, Nuclear Physics B, (1975)

[6] Second threshold in weak interactions, Veltman, MJG, Acta Phys. Pol. B, (1976)

[7] Limit on mass differences in the Weinberg model, Veltman, M, Nuclear Physics B, (1977)

[8] Study of (W/Z)H production and Higgs boson couplings using $H \to WW^*$ decays with the ATLAS detector, ATLAS collaboration and others, arXiv preprint arXiv: 1506.06641, (2015)

[9] Combined Measurement of the Higgs Boson Mass in pp Collisions at $\sqrt{s}$ = 7 and 8 TeV with the ATLAS and CMS Experiments, Collaborations, CMS, and others, arXiv preprint arXiv: 1503.07589, (2015)

[10] Charged Higgs pair production in a general two Higgs doublet model at e^+e^- and $\mu^+\mu^-$ linear colliders, author Hashemi, Majid, Communications in Theoretical Physics, (2014)

[11] Yukawa corrections to charged Higgs-boson pair production in photon-photon collisions, Ma, Wen-Gan and Li, Chong Sheng and Liang, Han, Physical Review D, (1996)

[12] New LHC benchmarks for the CP-conserving two-Higgs-doublet model, Haber, Howard E and Stål, Oscar, Eur. Phys. J. C (2015) 75: 491

[13] Searching for signs of the second Higgs doublet, Craig, Nathaniel and Galloway, Jamison and Thomas, Scott, arXiv preprint arXiv: 1305.2424, (2013)

[14] Natural conservation laws for neutral currents, Glashow, Sheldon L, and Weinberg, Steven, Physical Review D, (1977)

[15] Diagonal neutral currents, Paschos, Emmanuel A, Physical Review D, (1977)

[16] Theory and phenomenology of two-Higgs-doublet models, Branco, Gustavo Castelo and Ferreira, PM and Lavoura, L and Rebelo, MN and Sher, Marc and Silva, Joao P, Physics reports, (2012)

[17] PRINT-86-1324 (UC, DAVIS); JF Gunion, HE Haber, GL Kane and S. Dawson, Gunion, John F and Kayser, B, and Mohapatra, RN and Deshpande, NG and Grifols, J and Mendez, A and Olness, FI and Pal, PB, Front. Phys, (2000)

[18] Pattern of symmetry breaking with two Higgs doublets, Deshpande, Nilendra G and Ma, Ernest, Physical Review D, (1978)

[19] Search for microscopic black hole signatures at the Large Hadron Collider, CMS collaboration and others, arXiv preprint arXiv: 1012.3375, (2010)

[20] The global electroweak fit at NNLO and prospects for the LHC and ILC, Gfitter Group and Baak, M, and Cxuth, J and Haller, J and Hoecker, A and Kogler, Roman and Mönig, K and Schott, M and Stelzer, J, The European Physical Journal C, (2014)

[21] Search for heavy ZZ resonances in the final states using proton-proton collisions at TeV with the ATLAS detector, Aaboud, M and Aad, G and Abbott, B and Abeloos, B and Abidi, SH and AbouZeid, OS and Abraham, NL and Abramowicz, H and Abreu, H and Abreu, R and others, The European Physical Journal. C, Particles, and fields, (2018)

[22] collisions at $\sqrt{s}$ = 8 TeV with the ATLAS detector. Physics Letters B, 744, pp. 163-183. Copyright© 2015 CERN, for the ATLAS Collaboration., Aad, G, and others, Physics Letters B, (2015)

[23] Measurements of the Higgs boson production and decay rates and coupling strengths using pp collision data at *sqrts* = 7 and 8 TeV in the ATLAS experiment, Aad, Georges and Abbott, Brad and Abdallah, Jalal, and Aben, R and Abolins, M and AbouZeid, OS and Abramowicz, H and Abreu, H and Abreu, R and Abulaiti, Y and others, The European Physical Journal C, (2016)

[24] Updated next-to-next-to-leading-order QCD predictions for the weak radiative B-meson decays, Misiak, M and Asatrian, HM, Boughezal, Radja and Czakon, M and Ewerth, T and Ferroglia, A. and Fiedler, P. and Gambino, Paolo and Greub, Christoph and Haisch, U, and others, Physical review letters, (2015)

[25] Weak radiative decays of the B meson and bounds on $M_{H^\pm}$ in the Two-Higgs-Doublet Model, Misiak, Miko laj and Steinhauser, Matthias, The European Physical Journal C, (2017)

[26] Unitarity bound in the most general two Higgs doublet model, Kanemura, Shinya and Yagyu, Kei, Physics Letters B, (2015)

[27] Flavor constraints on the two Higgs doublet models of Z_2 symmetric and aligned types, Enomoto, Tetsuya and Watanabe, Ryoutaro, Journal of High Energy Physics, (2016)

[28] Bosonic decays of charged Higgs bosons in a 2HDM type-I, Arhrib, Abdesslam and Benbrik, Rachid and Moretti,

Stefano, The European Physical Journal C, (2017)

[29] Search for charged Higgs bosons decaying via $H^{\pm} \to \tau^{\pm}\nu$ in fully hadronic final states using pp collision data at s $\sqrt{s}$= 8 TeV with the ATLAS detector, Aad, Georges Abbott, B. and Abdallah, J and Abdel Khalek, S and Aben, R. and Abi, B. and Abolins, M and AbouZeid, OS and Abramowicz, H and Abreu, H and others, Journal of High Energy Physics, (2015)

[30] Search for a charged Higgs boson in pp collisions at $\sqrt{s}$= 8 TeV, Khachatryan, Vardan and Sirunyan, Albert M and Tumasyan, Armen and Adam, Wolfgang and Asilar, E and Bergauer, Thomas and Brandstetter, Johannes and Brondolin, Erica and Dragicevic, Marko and Erö, Janos and others, Journal of High Energy Physics, (2015)

[31] Search for a light-charged Higgs boson in the decay channel H+-GT c (s) over-bar in t (t) over-bar events using pp collisions at $\sqrt{s}$ = 7 TeV with the ATLAS detector, Aad, G and Borjanović, Iris and Božović-Jelisavčić, Ivanka and Ćirković, Predrag and Agatonović-Jovin, Tatjana and Krstić, Jelena x and Mamužić, Judita and Popović, DS and Sijackii, Dj and Simić, Lj and others, European Physical Journal C. Particles and Fields, (2013)

[32] Search for charged Higgs bosons: combined results using LEP data, ALEPH Collaboration, DELPHI Collaboration, L3 Collaboration, OPAL Collaboration, and LEP working group for Higgs boson searches, The European Physical Journal C, (2013)

[33] Prospects for charged Higgs searches at the LHC, Akeroyd, AG and Aoki, M and Arhrib, A and Basso, L and Ginzburg, IF and Guedes, R and Hernandez-Sanchez, J and Huitu, K and Hurth, T and Kadastik, M and others, The European Physical Journal C, (2017)

[34] 2HDMC–two-Higgs-doublet model calculator, Eriksson, David and Rathsman, Johan and St˚al, Oscar, Computer Physics Communications, (2010)

[35] Problems in obtaining $\gamma\gamma$ and γe colliding beams at linear colliders, Telnov, Valery I, Nuclear Instruments and Methods in Physics Research Section A: Accelerators, Spectrometers, Detectors and Associated Equipment, (1990)

[36] MadGraph 5: going beyond, Alwall, Johan and Herquet, Michel and Maltoni, Fabio and Mattelaer, Olivier and Stelzer, Tim, Journal of High Energy Physics, (2011)

[37] 2HDMC-a two Higgs doublet model calculator, Rathsman, Johan and St˚al, Oscar, arXiv preprint arXiv: 1104.5563, (2011)

[38] gnuplot 4.6, Williams, Thomas and Kelley, Colin and Bröker, Hans-Bernhard and Campbell, John and Cunningham, Robert and Denholm, David and Elber, Gershon and Fearick, Roger and Grammes, Carsten and Hart, Lucas and others, An Interactive Plotting Program, (2012)

[39] ROOT—An object-oriented data analysis framework, Brun, Rene and Rademakers, Fons, Nuclear instruments and methods in physics research section A: accelerators, spectrometers, detectors and associated equipment, 1997

[40] Boosted decision trees, Coadou, Yann, Artificial Intelligence for High Energy Physics, (2022)

[41] The toolkit for multivariate data analysis, TMVA 4, Speckmayer, P, and Höcker, A and Stelzer, J and Voss, H, Journal of Physics: Conference Series, (2010)

[42] An introduction to boosting and leveraging, Meir, Ron and Rätsch, Gunnar, Advanced Lectures on Machine Learning: Machine Learning Summer School 2002 Canberra, Australia, February 11–22, 2002 Revised Lectures, (2003)